

# The impact of assembly bias on the halo occupation in hydrodynamical simulations

M. Celeste Artale<sup>1,2\*</sup>, Idit Zehavi<sup>3</sup>, Sergio Contreras<sup>4,5</sup> & Peder Norberg<sup>6</sup>

<sup>1</sup>*Institut für Astro- und Teilchenphysik, Universität Innsbruck, Technikerstrasse 25/8, 6020 Innsbruck, Austria*

<sup>2</sup>*CONICET-Universidad de Buenos Aires. Instituto de Astronomía y Física del Espacio (IAFE), CC 67, Suc. 28, 1428 Buenos Aires, Argentina*

<sup>3</sup>*Department of Physics, Case Western Reserve University, 10900 Euclid Avenue, Cleveland, OH 44106, USA*

<sup>4</sup>*Instituto Astrofísica, Pontificia Universidad Católica de Chile, Santiago, Chile*

<sup>5</sup>*Centro de Estudios de Física del Cosmos de Aragón (CEFCA), Plaza San Juan 1, Planta-2, Teruel, E-44001, Spain*

<sup>6</sup>*ICC & CEA, Department of Physics, Durham University, South Road, Durham, DH1 3LE, UK*

2 August 2018

## ABSTRACT

We investigate the variations in galaxy occupancy of the dark matter haloes with the large-scale environment and halo formation time, using two state-of-the-art hydrodynamical cosmological simulations, EAGLE and Illustris. For both simulations, we use three galaxy samples with a fixed number density ranked by stellar mass. For these samples we find that low-mass haloes in the most dense environments are more likely to host a central galaxy than those in the least dense environments. When splitting the halo population by formation time, these relations are stronger. Hence, at a fixed low halo mass, early-formed haloes are more likely to host a central galaxy than late-formed haloes since they have had more time to assemble. The satellite occupation shows a reverse trend where early-formed haloes host fewer satellites due to having more time to merge with the central galaxy. We also analyse the stellar mass – halo mass relation for central galaxies in terms of the large-scale environment and formation time of the haloes. We find that low mass haloes in the most dense environment host relatively more massive central galaxies. This trend is also found when splitting the halo population by age, with early-formed haloes hosting more massive galaxies. Our results are in agreement with previous findings from semi-analytical models, providing robust predictions for the occupancy variation signature in the halo occupation distribution of galaxy formation models.

**Key words:** cosmology: galaxies – cosmology: theory – galaxies: formation – galaxies: haloes – galaxies: statistics – large-scale structure of universe

## 1 INTRODUCTION

In the current concordance  $\Lambda$ CDM paradigm, galaxies form and evolve in dark matter haloes. Studying the relation between galaxies and haloes is crucial for a better understanding of galaxy formation and for constraining cosmological models. Different methods have been developed to investigate this connection. In particular, a powerful technique to study the distribution of galaxies within dark matter haloes is the halo occupation distribution (HOD, e.g., Peacock & Smith 2000; Seljak 2000; Scoccimarro et al. 2001; Berlind & Weinberg 2002). The occupation function is defined as the average number of galaxies that populate a halo as a function of halo mass,  $\langle N(M_h) \rangle$ . In other

words, the HOD is computed by the probability distribution  $P(N|M_h)$ , which represents the probability that a halo of mass  $M_h$  hosts  $N$  galaxies with certain selected properties. The HOD approach has shown to be useful for interpreting galaxy clustering measurements and constraining models of galaxy formation (e.g., Benson et al. 2000; Zentner et al. 2005; Zehavi et al. 2011). The standard HOD scheme assumes that the galaxy population depends solely on the mass of the dark matter halo, motivated by the excursion set formalism. However, this assumption might be inaccurate if the galaxy population within haloes depends on additional halo properties.

It is currently well established in  $\Lambda$ CDM simulations that the spatial clustering of dark matter haloes depends on different halo properties besides their mass. This dependence is commonly referred to as *halo assembly bias*. Dif-

\* E-mail: Maria.Artale@uibk.ac.at, mcartale@gmail.com

ferent studies have investigated the dependence with varied halo properties such as their formation time, accretion rate, spin, shape, velocity dispersion, concentration and anisotropy (e.g., Sheth & Tormen 2004; Avila-Reese et al. 2005; Gao et al. 2005; Wechsler et al. 2006; Gao & White 2007; Faltenbacher & White 2010; Sunayama et al. 2016; Mao et al. 2018). The origin of halo assembly bias is still unclear, although different explanations have been proposed. One possible mechanism is described by Hahn et al. (2009), where they suggest that low mass haloes in filaments are driven by tidal suppression of the halo growth rate in the vicinity of a neighbouring massive halo. Also long wavelength modes might affect the halo formation times, and prevent the uncorrelated random walks adopted by the excursion set model (Zentner 2007; Dalal et al. 2008).

If the galaxy properties closely correlate with the halo formation history, halo assembly bias might also be reflected in the galaxy distribution. We refer to that effect as *galaxy assembly bias* (e.g., Zhu et al. 2006; Croton et al. 2007; Reed et al. 2007; Zu et al. 2008; Chaves-Montero et al. 2016; Zehavi et al. 2018). If this is the case, the standard HOD formalism would be incomplete and different complex approaches should be considered (Zentner et al. 2014; Hearin et al. 2016a). However, the observational and theoretical evidence for the existence of galaxy assembly bias is still controversial and under debate. From the observational point of view, different studies claim a detection of this effect (e.g., Yang et al. 2006; Wang et al. 2008, 2013; Lacerna et al. 2014; Miyatake et al. 2016; Montero-Dorta et al. 2017; Tinker et al. 2017; Tojeiro et al. 2017), while other works show small or negligible impact on galaxy properties (e.g., Blanton & Berlind 2007; Tinker et al. 2008; Vakili & Hahn 2016; Dvornik et al. 2017), or systematics in the previously claimed detections (e.g., Campbell et al. 2015; Zu et al. 2017; Tinker et al. 2018).

A way to study the theoretical predictions for galaxy assembly bias is through the analysis of different galaxy formation models. Previous reports have explored galaxy assembly bias in semi-analytic models and hydrodynamical cosmological simulations. For instance, Croton et al. (2007) demonstrate the existence of galaxy assembly bias in a semi-analytical model applied onto the Millennium Simulation, by comparing the two-point correlation functions from the model galaxies with a shuffled version, where assembly bias is erased. Chaves-Montero et al. (2016) do a similar analysis in the EAGLE simulation, finding an even stronger effect. Using galaxies in the Illustris simulation, Bray et al. (2016) detect a significant signal of galactic conformity (i.e., the correlation between star formation and colour of central galaxies and their neighbours; see Kauffmann et al. 2013), a signature that has been linked to assembly bias (Hearin et al. 2015, 2016b).

The subhalo abundance matching technique (SHAM) is another useful method to consider when discussing galaxy assembly bias signatures. SHAM connects dark matter substructures with galaxies using a direct relation between a galaxy property such as its stellar mass or luminosity, and a subhalo property like its infall subhalo mass or its maximum circular velocity (Conroy et al. 2006; Reddick et al. 2013; Mao et al. 2015; Chaves-Montero et al. 2016; Lehmann et al. 2017; Dragomir et al. 2018).

Signatures of galaxy assembly bias can be studied by directly exploring how the halo occupation might depend (or not) on different halo properties. Following Zehavi et al. (2018), we refer to this dependence as *occupancy variation*. The occupancy variation was studied previously in different galaxy formation models. Berlind et al. (2003) and Mehta (2014) investigate the environmental variations of the HOD in hydrodynamical cosmological simulations, finding no significant signals of this dependence. McEwen & Weinberg (2018) use the age-matching catalogues of Hearin & Watson (2013) which exhibit by construction strong galaxy assembly bias signal, to explore the dependence of HOD with environment. Their findings suggest this dependence exist mainly for central galaxies. Most recently, Zehavi et al. (2018) investigate the dependence of the halo occupancy on large-scale environment and halo formation time, by using two different semi-analytic galaxy formation models implemented in the Millennium simulation. Their results show distinct features of occupancy variation. Central galaxies in high dense large-scale environments are more likely to reside in lower-mass haloes. A much stronger signal is found with halo formation time, where early-forming low mass haloes are more likely to host a central galaxy. Furthermore, they find a reverse trend for the satellite galaxies, with early-forming haloes containing less satellites.

In this work, we extend the investigation presented in Zehavi et al. (2018) with semi-analytical models, to analyse the impact of the occupancy variation reflected in the state-of-the-art hydrodynamical cosmological simulations EAGLE and Illustris (Schaye et al. 2015; Vogelsberger et al. 2014). For this purpose, we analyse the HOD and its dependence on the halo formation redshift, and the large-scale environment of the haloes. We explore the trends for three different number densities with galaxies ranked by their stellar mass, when selecting 20% of the haloes in the most and least dense environments and the 20% youngest and oldest haloes.

This paper is organised as follows. In § 2 we present a brief overview of the main features of the EAGLE and Illustris simulations. In § 3 we provide the definitions adopted to construct the samples according to halo environment and formation time. Our findings are presented in § 4, and the halo occupancy variation in the context of the stellar mass – halo mass relation is discussed in § 5. The main conclusions are summarised in § 6. We discuss our large-scale environment definition in Appendix A, and we characterise the HOD of galaxies (stellar mass ranked) from EAGLE and Illustris in Appendix B. We analyse the occupancy variation in the context of subhaloes in Appendix C.

## 2 THE HYDRODYNAMICAL SIMULATIONS

In this section we describe the main relevant properties of the hydrodynamical cosmological simulations EAGLE and Illustris used in this work, and our samples selection. We note that the cosmological parameters adopted for each simulation are different (see below).

### 2.1 The EAGLE hydrodynamical simulation

The EAGLE simulation suite (Schaye et al. 2015; Crain et al. 2015) is a set of cosmological hydrodynamical simulations

performed with a modified version of GADGET-3 code (based on GADGET-2, see Springel 2005). It is composed by different runs where the resolution and box sizes are varied, starting from  $z = 127$  up to  $z \sim 0$ , and adopting the  $\Lambda$ CDM cosmology with parameters inferred from Planck Collaboration et al. (2014)<sup>1</sup>. The hydrodynamical cosmological simulations uses sub-grid physics to describe the physical processes that are below their resolution limit. For the case of the EAGLE suite, the sub-grid physics is based on that developed for OWLS and GIMIC simulations (Schaye et al. 2010; Crain et al. 2009, respectively).

Here we describe briefly the most important aspects of the sub-grid physics implemented in the EAGLE suite. Star formation follows the pressure-dependent Kennicutt-Schmidt relation from Schaye & Dalla Vecchia (2008) and the metallicity-dependent density threshold of Schaye (2004). Therefore, gas particles that fulfil the condition for star formation are converted to a collisionless star particle stochastically with a probability which depends on the time step and the star formation rate. Radiative cooling and heating are implemented element-by-element adopting the model described in Wiersma et al. (2009a). UV/X-ray ionizing background is included from Haardt & Madau (2001) at  $z = 11.5$  consistent with the measurements from Planck Collaboration et al. (2014). Stellar evolution and chemical enrichment is implemented following Wiersma et al. (2009b) and adopting a Chabrier (2003) initial mass function in the mass range of  $[0.1, 100] M_{\odot}$ . In this way, the simulation tracks the stellar mass loss and enrichment of the interstellar medium from AGB stars, type II (core collapse) supernovae, and type Ia supernovae. Thermal feedback from stars is implemented following the stochastic method described in Dalla Vecchia & Schaye (2012). Black holes seeds are located in haloes more massive than  $10^{10} h^{-1} M_{\odot}$  and are tracked (merging and accretion) following Springel et al. (2005); Booth & Schaye (2009). The model also includes the gas accretion onto black holes with a modified version of the Bondi-Hoyle accretion rate described in Rosas-Guevara et al. (2015). Thermal feedback from accreting black holes is also implemented stochastically (see Schaye et al. 2015).

The EAGLE suite of simulations are tuned to reproduce the galaxy stellar mass function, galaxy sizes and the relation between the stellar mass and black hole mass (Shen et al. 2003; Baldry et al. 2012). The simulation also reproduce a wide variety of observables that are not tuned such as the specific star formation rates, the Tully-Fisher relation, the stellar luminosities of galaxy clusters, the luminosity function and colour-magnitude diagram at  $z = 0$  (Trayford et al. 2015) and the evolution of the galaxy stellar mass function (Furlong et al. 2015). Furthermore, the galaxy clustering within the EAGLE simulation was also studied in Chaves-Montero et al. (2016) and Artale et al. (2017) finding good agreement with observations at small scales.

In this work, we use the galaxy catalogues at  $z = 0$  of the simulation named as L0100N1504 from the EAGLE suite (hereafter we refer to this run as EAGLE<sup>2</sup>), which

are available on their SQL database (see McAlpine et al. 2016). This run consists of a periodic box of  $67.77 h^{-1} \text{Mpc}$  (100 Mpc) side, which initially contain  $1504^3$  of gas and dark matter particles, with masses of  $m_{\text{gas}} = 1.23 \times 10^6 h^{-1} M_{\odot}$  and  $m_{\text{DM}} = 6.57 \times 10^6 h^{-1} M_{\odot}$ .

## 2.2 The Illustris hydrodynamical simulation

The Illustris Project (Vogelsberger et al. 2014; Genel et al. 2014) is a set of cosmological hydrodynamical simulations of periodic  $(75 h^{-1} \text{Mpc})^3$  volume that was performed with the AREPO moving-mesh code of Springel (2010). The simulations were run following the evolution of dark matter, gas and star particles with three different resolution levels from  $z = 127$  to  $z = 0$  within a  $\Lambda$ CDM cosmological scenario<sup>3</sup>.

The Illustris simulations also include sub-grid models for those physical processes out of the resolution limits of the simulation (for further details see, Vogelsberger et al. 2013). Star formation is implemented following Springel & Hernquist (2003), where gas particles are promoted to star stochastically when their density is above a certain limit within a star formation time-scale. Stellar evolution and chemical enrichment are implemented adopting the Chabrier (2003) initial mass function in the same mass range than in EAGLE. Therefore, the model follows the mass loss and chemical contribution into the interstellar medium from AGB stars, core collapse supernovae and Type Ia supernovae. Radiative cooling is implemented through spatially uniform time-dependent UVB and metal-line cooling based on CLOUDY (see Vogelsberger et al. 2013). Stellar winds and supernovae feedback are implemented following an adapted model from Springel & Hernquist (2003). The seed of black holes are located in dark matter haloes with masses above  $5 \times 10^{10} h^{-1} M_{\odot}$ , and active galactic nuclei feedback implementation follow previous studies (Di Matteo et al. 2005; Springel et al. 2005).

In Illustris the free parameters from the sub-grid models were tuned to reproduce the cosmic star-formation rate density and the stellar mass function at  $z = 0$  in a smaller volume of  $\sim 25 h^{-1} \text{Mpc}$  (35.5 Mpc) of a side. This simulation has also shown to reproduce different observed properties that are not tuned such as the distribution of the galaxy morphologies (Snyder et al. 2015), the build-up of galactic mass, the evolution of galaxy specific star formation rates up to  $z = 8$  (Genel et al. 2014) and the colours of satellites (Sales et al. 2015). However, some observational properties are not well reproduced such as the galaxy stellar mass function for the  $75 h^{-1} \text{Mpc}$  side box, finding at  $z \sim 0$  an excess of galaxies at high and low stellar masses (see Vogelsberger et al. 2014).

The Illustris project provides open access to their database<sup>4</sup>, where it is possible to obtain information about the particle and galaxy catalogues at different redshifts (see, Nelson et al. 2015). In this work we use Illustris-1, the highest resolution simulation run which initially contains  $1820^3$  gas and dark matter particles with masses of  $m_{\text{gas}} = 1.13 \times 10^6 h^{-1} M_{\odot}$  and  $m_{\text{DM}} = 4.44 \times 10^6 h^{-1} M_{\odot}$ .

<sup>1</sup>  $\Omega_m = 0.2588$ ,  $\Omega_{\Lambda} = 0.693$ ,  $\Omega_b = 0.0482$ ,  $\sigma_8 = 0.8288$ ,  $n_s = 0.9611$ , and  $H_0 = 100 h \text{ km s}^{-1} \text{ Mpc}^{-1}$  with  $h = 0.6777$ .

<sup>2</sup> <http://icc.dur.ac.uk/Eagle/>, <http://virgo.dur.ac.uk/data.php>

<sup>3</sup>  $\Omega_m = 0.2726$ ,  $\Omega_{\Lambda} = 0.7274$ ,  $\Omega_b = 0.0456$ ,  $\sigma_8 = 0.809$ ,  $n_s = 0.963$ , and  $H_0 = 100 h \text{ kms}^{-1} \text{ Mpc}^{-1}$  with  $h = 0.704$ .

<sup>4</sup> <http://www.illustris-project.org>

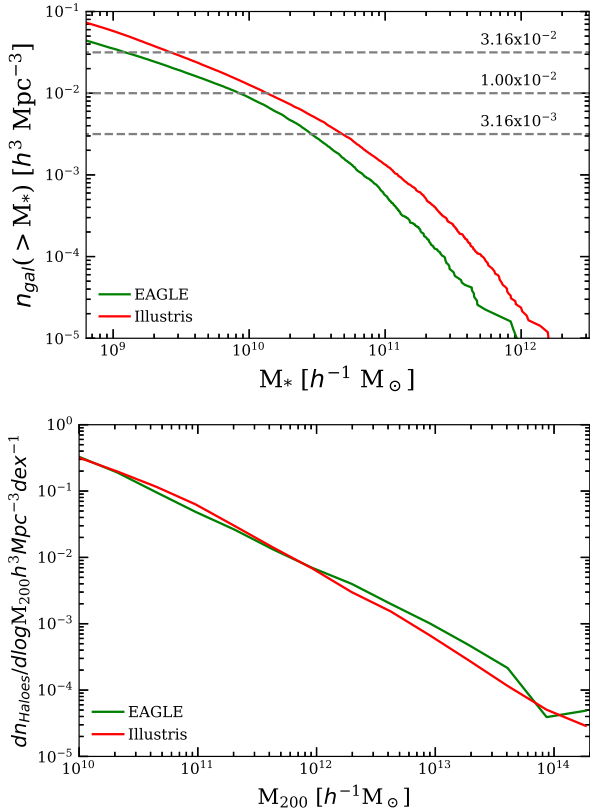


**Figure 1.** *Top panel:* The cumulative stellar mass function of EAGLE (green line) and Illustris (red line). The dashed lines represent the galaxy number densities selected to estimate the HOD corresponding to  $n = (0.0316, 0.01, 0.00316) h^3 \text{ Mpc}^{-3}$ . *Bottom panel:* Halo mass functions of EAGLE (green line) and Illustris (red line). We use  $M_{200}$  as the halo mass.

An updated version of the physical model implemented was recently published improving some of the issues mentioned above. This new version, known as IllustrisTNG (Springel et al. 2018; Pillepich et al. 2018), includes the effect of seed magnetic fields, an updated model for galactic winds and a new implementation of supermassive black holes kinetic feedback. Once publicly available, it would be interesting to revisit our analysis using the improved IllustrisTNG simulation.

### 2.3 Selection of galaxies and dark matter haloes

In both simulations the dark matter haloes are identified using the *Friends-of-Friends* (FoF) method on the dark matter only simulation with a linking length of 0.2 times the mean interparticle separation (Davis et al. 1985). Gravitationally bound substructures (or subhaloes) within haloes are identified using the SUBFIND algorithm (Springel et al. 2001) in both simulations. The SUBFIND algorithm uses the gas, stellar and dark matter particles assigned to each FoF halo (Schaye et al. 2015). Galaxies are associated with the baryonic component within each subhalo. Central and satellite galaxies are identified and provided by the simulation teams. In EAGLE, the central galaxy resides in the subhalo that contains the most bound dark matter particle in the halo,

while the remaining subhaloes host the satellite galaxies (see McAlpine et al. 2016). On the other hand, in the Illustris simulation, central and satellite galaxies are labelled by the mass of the subhaloes, where the most massive one hosts the central galaxy.

We note that small subhaloes may not contain stellar and/or gas particles even at  $z \sim 0$ . We use the full sample of the subhaloes to define the environment of the haloes, irrespective of whether they contain a galaxy or not (see § 3.1 for further details). In this work we use the following information provided by the database of each simulation: the stellar mass of the galaxies ( $M_*$ ), the mass of the halo ( $M_{200}$ ) defined as the total mass (i.e., the sum over dark matter and baryonic mass) enclosed within a sphere with a density equal to 200 times the critical density, and the co-moving positions of the galaxies<sup>5</sup>.

We also use the information supplied by the subhalo merger trees to define the formation time of the dark matter haloes (see § 3.2). In the case of EAGLE the descendant subhaloes are identified using the D-TREES algorithm (Jiang et al. 2014; Qu et al. 2017), which traces the subhaloes using the most bound particles of any species. The main progenitor branch is defined as the progenitor with the largest mass in each redshift. For Illustris, the merger trees are computed using three different algorithms: SUBLINK (Rodríguez-Gomez et al. 2015), LHALOTREE (Springel et al. 2005) and CONSISTENT-TREES using ROCKSTAR (Behroozi et al. 2013). Here we use the subhalo merger tree computed with SUBLINK, available in the database. We also use the main branch defined as the one with the most massive history.

We present the cumulative comoving number density of galaxies for EAGLE and Illustris in the top panel of Fig. 1 (green and red lines, respectively). The Illustris simulation contains more massive galaxies than the EAGLE simulation, which is mainly explained by the differences in the sub-grid model for feedback from star-formation (see Schaye et al. 2015). In the bottom panel of Fig. 1 we present the halo mass functions for both simulations. We generally find a good agreement, while at high halo masses, haloes in EAGLE are more numerous than in Illustris. This is consistent with sample variance expected from the size of the boxes used (Artale et al. 2017).

To analyse the occupancy variation, we adopt criteria to select dark matter haloes according to their formation time or environment. We use three different number density samples, ranking galaxies by stellar mass, corresponding to  $n = (0.0316, 0.01, 0.00316) h^3 \text{ Mpc}^{-3}$ . These are denoted in the top panel of Fig. 1 by the dashed lines (see Sec. 4.1, for further discussion regarding the selected samples).

## 3 HALO SAMPLES

In this work we investigate the occupancy variation of the HOD with halo formation time and large-scale environment. We first select the dark matter haloes with  $M_{200} > 10^{10} h^{-1} M_{\odot}$  and their respective subhaloes at  $z = 0$ . We

<sup>5</sup> The co-moving position of a galaxy is defined as the minimum of the gravitational potential, as defined by the most bound particle.

note that the halo mass functions are slightly different between EAGLE and Illustris (see § 4.1 and Fig. 1). Those differences need to be accounted for when making a direct comparison of the HOD findings from each simulation.

In the case of EAGLE simulation, the mean number density of selected haloes that fulfill the halo mass condition is  $\sim 0.16 h^3 \text{Mpc}^{-3}$ , while for Illustris it is  $\sim 0.2 h^3 \text{Mpc}^{-3}$ . It is important to consider the cosmic variance among the two simulations. Artale et al. (2017) studied in detail the impact of cosmic variance on the two-point galaxy correlation function from the two simulations. The halo mass cut is adopted conforming to the resolution limits of the simulations, in order to have more than  $\sim 1500$  dark matter particles within each halo. This is valid for both simulations. In this section, we present the definitions implemented for the halo formation time and the large-scale environment and how we split the halo populations by these properties in order to study the occupancy variation.

### 3.1 Selection by large-scale environment

We investigate the occupancy variation due to the large-scale environment. We define the large-scale environment of each dark matter halo by counting all the subhaloes within a sphere of  $5 h^{-1} \text{Mpc}$  radius (excluding those that belong to the same halo), divided by the volume of the sphere, and adopting periodic boundary conditions (we denote this environment measure as  $n_{5\text{Mpc}/h}$ ).

We note that we are counting subhaloes and not galaxies, since some subhaloes may not contain gas and/or stellar particles (see § 2.3). For both simulations we use all the subhaloes provided by each database that belong to the selected haloes (see McAlpine et al. 2016; Nelson et al. 2015, for further details). Hence, the environment definition adopted depends on the resolution limit of each simulation. While this should be taken into account in future comparisons, we do not expect this to significantly impact our main results.

We normalize this quantity by the number density of subhaloes within haloes of  $M_{200} > 10^{10} h^{-1} M_{\odot}$  (referred to  $n_{\text{avg}}$ ). We tested different radii for the sphere (see Appendix A for more details). We select a radius of  $5 h^{-1} \text{Mpc}$  to quantify the environment as a compromise between covering volumes larger than those of the biggest haloes, but also taking into account the size of the simulated box. The test with other radii gives us similar results, making our findings robust.

Similar to the method implemented in Zehavi et al. (2018), to classify the dark matter haloes according to their environment, we display the halo masses in bins of  $\sim 0.24$  dex and select those with the 20% most and least dense environment in each halo mass bin. We define environment cuts separately in bins of halo mass to factor out the halo mass function dependence on environment. Therefore, with this approach it is possible to compare the differences in the HOD at fixed halo mass and different environments. Additionally, all the samples will have, by definition, the same halo mass function.

We show the spatial distribution of the dark matter haloes for a slice of the EAGLE (top) and Illustris (bottom) simulations in the left hand of Fig. 2, split by those in the most and least dense environments marked by red and blue points, respectively. Black points show those haloes in the

slice not included in these selections. As expected, we find that the haloes from each population map different regions of the large-scale structure, where the haloes from the high density population are distributed in more compact and clustered regions than the haloes from the low dense population.

The left panel of Fig. 3 show the selection criteria of the EAGLE haloes for the most and least dense environment (red and blue points). Black points correspond to those haloes that do not belong to the selected populations. We find that the density cut selected to define the haloes in the most and least dense environments gradually increases with halo mass, reflecting the well-known dependence of the halo mass function on environment. The median value also shows an increase with halo mass as expected.

### 3.2 Selection by halo formation time

To classify the haloes according to their assembly history, we compute the formation time of the haloes ( $z_{\text{form}}$ ), as the redshift at which for the first time half of present-day halo mass has been accreted into a single subhalo. For this purpose, we use the subhalo merger trees of each simulation to track the mass since  $z = 6$ . For all the haloes that at  $z = 0$  have a mass  $M_{200} > 10^{10} h^{-1} M_{\odot}$ , we follow the progenitors of the main branch. We compute the formation redshift using a spline interpolation of the masses.

To classify the haloes, we identify the 20% early-formed (old haloes) and the 20% late-formed (young haloes), in fixed bins of 0.24 dex of halo mass. The spatial distribution of the dark matter haloes for a slice of each simulation is shown in the right side of Fig. 2 (EAGLE on top, and Illustris on bottom). Red points correspond to the dark matter haloes that belong to the sample of 20% early-formed, while blue points correspond to the 20% late-formed. We find that the population of early and late formed haloes map different regions of the cosmic web, and the spatial distribution is different to the one split by environment. This suggests that the two methods to classify halo populations are not strongly correlated (see more below in this section).

The right panel of Fig. 3 presents the corresponding selection criteria for the EAGLE haloes for the 20% early-formed and late-formed haloes (red and blue points). Black points are those haloes that do not belong to any of these populations, while the yellow line is the median of the formation time for each halo mass bin. The population of early-formed haloes show a wide range of formation redshifts between  $z \sim 1 - 6$  as function of halo mass, while late-formed haloes are generally below  $z \sim 1$  for all halo masses. The median formation time decreases with increasing halo mass, reflecting the late formation time of massive haloes.

As already mentioned, the visual comparison of the haloes' spatial distribution in Fig. 2 shows that each criterion roughly selects a distinct distribution, where haloes selected by age and environment are not strongly correlated. To quantify how independent these subsamples are, we compute the fraction of haloes that are in common in young/low-density and old/high-density selections. We find that approximately 25% – 30% of the young (old) subsample of haloes belong also to low-density (high-density) haloes for EAGLE and Illustris (this corresponds to  $\sim 5\%$  of the total dark matter haloes with  $M_{200} > 10^{10} h^{-1} M_{\odot}$ ).

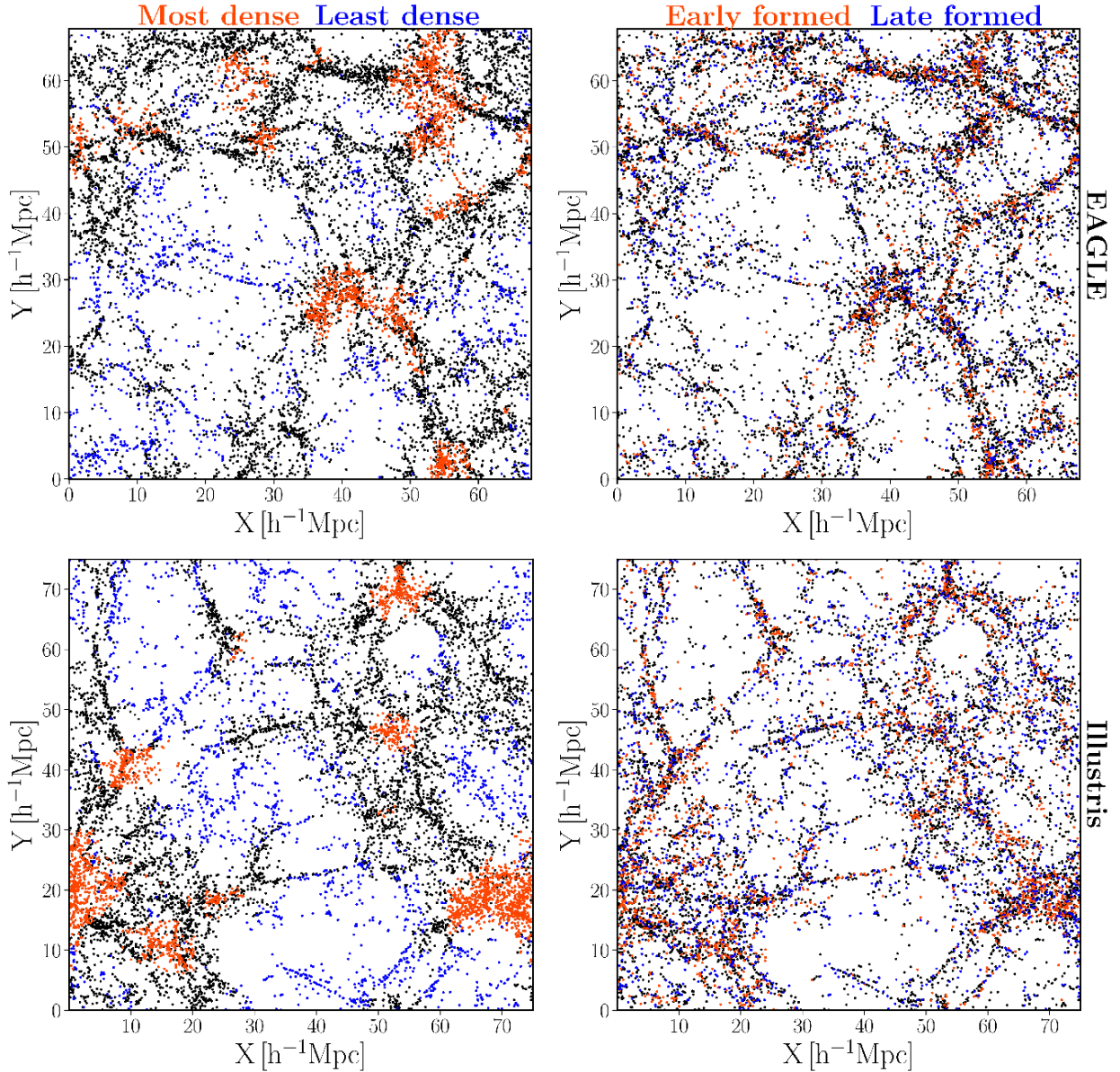


**Figure 2.** Spatial distribution of the dark matter haloes split by environment (*left panel*) and formation time (*right panel*) for haloes with masses  $M_{200} > 10^{10} h^{-1} M_{\odot}$ . We present a slice of  $67.7 \times 67.7 \times 10 h^{-1}$  Mpc of the EAGLE simulation (*top panels*), and a slice of  $74.9 \times 74.9 \times 10 h^{-1}$  Mpc for Illustris simulation (*bottom panels*). In each case, the x and y ranges shown correspond to the maximum comoving length of each simulation. In the left panels, red and blue dots represent 20% of the haloes in the most and least dense environments, respectively. In the right panels, red dots represent the haloes that belong to the 20% earliest-formed (oldest) haloes, while the blue dots are the 20% latest-formed (youngest) haloes. Black points show haloes not belonging to any of the two selected populations. See § 3 for more details.

We also analyse the differences in halo selection for the full halo sample. Fig. 4 shows the correlation of formation time with the large-scale environment in EAGLE for three different mass bins (similar to the analysis presented in Fig. 2 of Zehavi et al. 2018). For each halo mass bin, we show the median values of the environment as a function of formation redshift (vertical lines) and the median values of the formation time as a function of large-scale environment (horizontal lines). We find a slight trend of early-formed haloes residing in denser environments, as indicated by the slanted lines. However, overall we find a broad range of halo formation times and densities, suggesting that there is little

correlation between these quantities. It is thus interesting to investigate the occupancy variation of these two largely independent quantities.

#### 4 THE OCCUPANCY VARIATION

In this section we present our results for the occupancy variation with large-scale environment and halo age. We first compare the HOD of EAGLE and Illustris for three samples with different galaxy number densities and analyse the differences in the central and satellite galaxy populations. We

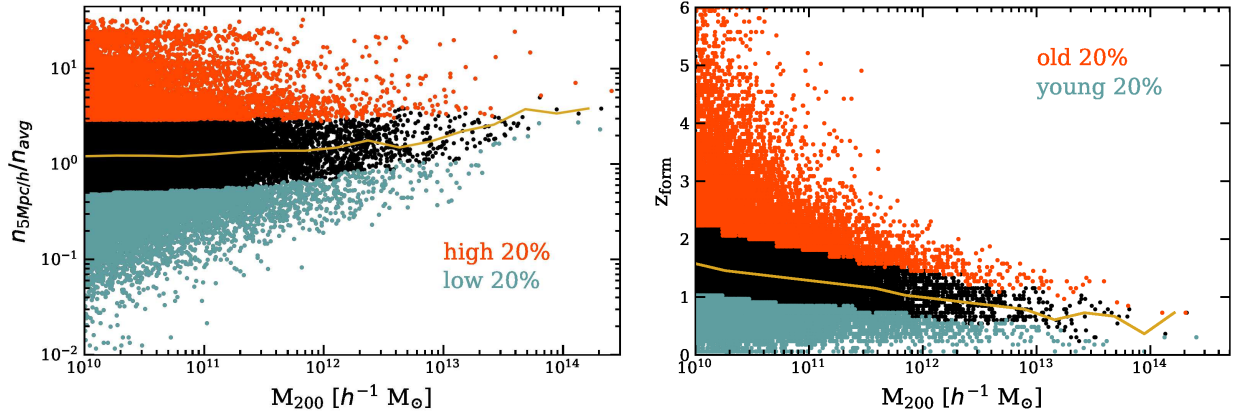


**Figure 3.** *Left panel:* The distribution of large-scale environment with halo mass, showing the different environment regions used in this work. We show the dark matter haloes with  $M_{200} > 10^{10} h^{-1} M_{\odot}$  from the EAGLE simulation. We split the population into 20% highest (red points) and lowest (blue points) density environments for each halo mass bin. Black points are the haloes that do not belong to any of the selected samples. The yellow line represents the median large-scale environment for each halo mass bin. *Right panel:* The same as the left panel, but for the formation time of the haloes ( $z_{\text{form}}$ ), as a function of halo mass for EAGLE split by the 20% latest-formed (blue) and earliest-formed (red) haloes for each halo mass bin.

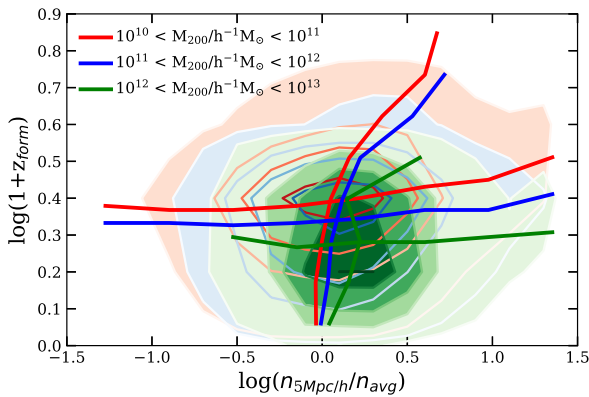


**Figure 4.** Joint distribution of the large-scale environment ( $n_{5\text{Mpc}/h}/n_{\text{avg}}$ ) and formation time ( $1 + z_{\text{form}}$ ) for dark matter haloes of the EAGLE sample. The contours correspond to enclosing 20, 50, 70, 95 per cent of the sample for three different halo mass ranges:  $10^{10} - 10^{11} h^{-1} M_{\odot}$  (red),  $10^{11} - 10^{12} h^{-1} M_{\odot}$  (blue),  $10^{12} - 10^{13} h^{-1} M_{\odot}$  (green). The roughly vertical lines represent the median values of the environment at each formation redshift and halo mass bin, while horizontal lines correspond to the median values of the formation redshift as a function of the large-scale environment.

then study how the HOD varies with the large-scale environment and halo formation time. We clarify that while each selected subset of haloes represent 20% of the haloes at  $z = 0$  with  $M_{200} > 10^{10} h^{-1} M_{\odot}$ , the associated galaxies do not necessarily make up the same fraction.

#### 4.1 The halo occupation distribution

We first compare the HOD of EAGLE and Illustris for fixed number density samples ranked by galaxy stellar mass. This approach has shown to be a preferred alternative to fixed stellar mass samples since it is not affected by systematic shifts in the stellar mass estimates and model calibrations

(e.g., Padilla et al. 2011; Contreras et al. 2013; Leja et al. 2013; Mitchell et al. 2013; Mundy et al. 2015; Torrey et al. 2015).

The cumulative comoving number density of galaxies ranked as a function of stellar mass with the three cuts adopted was shown already in Fig. 1. The number densities selected are  $n = (0.0316, 0.01, 0.00316) h^3 \text{Mpc}^{-3}$  for both simulations. From Fig. 1 it is evident that each number density chosen corresponds to a different stellar mass cut for each simulation, reflecting the variations between the galaxy formation models and the model tuning adopted.

The left panel of Fig. 5 presents the HODs obtained from EAGLE (green lines) and Illustris (red lines) for the three number densities. We find that the mean occupation of haloes in Illustris is shifted towards lower halo masses relative to EAGLE. This can be explained by the differences in halo mass functions seen in Fig. 1 (*bottom panel*). Since EAGLE contains a larger number of massive dark matter haloes relative to Illustris, this translates to a shift in the occupation of the dark matter haloes. We also show the HOD split by central and satellite galaxies in the right panel of Fig. 5, for the galaxy samples of EAGLE and Illustris at  $n = 0.0316 h^3 \text{Mpc}^{-3}$  finding similar results for both simulations. We provide parametrized fits to the HOD from EAGLE and Illustris in Appendix B. This may be useful for contrasting with different galaxy formation models or observational results in the future.

As stated earlier, we investigate the HOD in EAGLE and Illustris using the masses of dark matter haloes from the hydrodynamical simulations. However, we note that HOD analyses are typically based on dark matter only simulations (DMO). It is well known that baryons modify the properties of their dark matter hosts (e.g., Pedrosa et al. 2010; Tissera et al. 2010; Di Cintio et al. 2014; Schaller et al. 2015; Dutton et al. 2016). Hence, the HOD might present differences when using the halo masses from the hydrodynamical and/or DMO counterpart. Chaves-Montero et al. (2016) find only negligible impact in the two-point correlation function of central galaxies when the sample is selected

using the maximum circular velocity from the full EAGLE simulation or their DMO counterpart. Therefore, we expect this to only have a minor impact on our results.

In the following sections, we compare the occupancy variations of Illustris and EAGLE galaxies for the three number densities presented, with environment and halo formation time.

#### 4.2 The HOD dependence on environment

In Fig. 6 we present the HOD as a function of environment for our three number density cuts  $n = (0.0316, 0.01, 0.00316)h^3 \text{ Mpc}^{-3}$ . We obtain jack-knife error bars for the HOD of the galaxy samples for the most/least dense regions by using 27 sub-volumes of the full simulated boxes. We limit the halo mass range below  $M_{200} \sim 3.5 \times 10^{13} h^{-1} M_{\odot}$  in order to have at least ten dark matter haloes per mass bin.

In both simulations at low halo masses ( $M_{200} \lesssim 10^{12} h^{-1} M_{\odot}$ ) we find clear signatures of occupancy variation in the turnover of the central HOD, where the high density environments more likely to host a central galaxy than those in low dense environments. The trend is more significant in EAGLE than Illustris for all number densities. The occupancy variation reduces for the massive haloes, where haloes in most and least dense environments show a similar mean number of galaxies.

In Fig. 6 we also show the satellite HOD (dashed lines) for the complete sample and for the haloes in the most and least dense environments. For the number density of  $n = 0.0316 h^3 \text{ Mpc}^{-3}$ , we find that the haloes in the densest regions from EAGLE and Illustris shift toward lower halo mass, like the central occupancy variation. This may be a consequence of the densest environments favouring halo interactions and mergers. However, this trend is not clear for the other number densities studied, possibly due to the limitations of the simulated volumes. The error bars in Illustris are much narrower than EAGLE. This might be due to haloes in the densest environments being more uniformly distributed in Illustris (from an inspection by eye of Fig. 2). Finally, both simulations suggest that besides their mass, the halo occupation depends on the large-scale environment, in agreement with recent findings (McEwen & Weinberg 2018; Zehavi et al. 2018) but in contrast to some earlier studies with hydrodynamical simulations (Berlind et al. 2003; Mehta 2014).

#### 4.3 The HOD dependence on halo formation time

Fig. 7 presents the HOD for EAGLE and Illustris for the complete sample of each number density and for the galaxy populations in the 20% early-formed and late-formed haloes. We include error bars for the galaxy samples in the early-formed and late-formed haloes (red and blue lines, respectively) computed using jack-knife resampling using 27 sub-volumes of each full simulated box.

Both simulations show that at low masses, the oldest haloes are more likely to host a galaxy than the youngest haloes. This effect is mostly apparent in the ‘‘turnover’’ of the centrals occupation function. We find that this result is clearer for EAGLE than Illustris. This trend reverses for

high mass haloes (above  $\sim 10^{12} h^{-1} M_{\odot}$ ), where young haloes have on average a larger number of galaxies than old haloes. This is explained by the satellites occupation shown as well in Fig. 7 as dashed lines. We see that the oldest haloes tend to host fewer satellite galaxies, likely since they had more time to merge with the central galaxies. This trend is found in both simulations and more clear for the intermediate and highest number densities. Our findings are also in agreement with those from subhalo occupation split by halo formation time (van den Bosch et al. 2005; Mao et al. 2015; Jiang & van den Bosch 2017, see Appendix C for further discussions regarding this aspect). Also Garaldi et al. (2018) using zoom-in hydrodynamical simulations find that the fraction of mass in substructures is substantially larger in accreting (late forming) haloes.

We find in both EAGLE and Illustris, that the variations in the HOD are stronger when split by formation time compared to a split on environment. This is again in agreement with Zehavi et al. (2018) who found similar results in two semi-analytic models. Hence, together with the previous findings, our results support the notion that the formation time is a more fundamental property to describe the occupancy variation.

## 5 THE STELLAR MASS - HALO MASS RELATION

The trends we find in the halo occupation with large-scale environment and formation time of the haloes can also be discussed in the context of the stellar mass – halo mass relation (SMHM) for central galaxies. Following Zehavi et al. (2018), we show in Fig. 8 the SMHM dependence on environment for EAGLE (*left*) and Illustris (*right*). The black thin line shows the median value of the distribution, with error bars representing the 20% and 80% percentiles exhibiting, as expected, the stellar mass increase with halo mass.

The SMHM in both simulations shows a change in the slope at a halo mass of  $M_{200} \sim 10^{12} h^{-1} M_{\odot}$ , as a consequence of the contribution from the different feedback mechanisms (supernovae and AGN feedback) and merger mechanisms to the stellar mass of galaxies (see, e.g., Matthee et al. 2017). This change in the slope is clearer for EAGLE than Illustris. The dispersion of the SMHM is dependent on halo mass, where dark matter haloes below to  $\sim 10^{12} h^{-1} M_{\odot}$  present a larger range of stellar masses for the central galaxies. As discussed in Matthee et al. (2017), the dispersion at a fixed halo mass might be due to differences in the halo concentration which in turn is related with their formation times.

The central galaxies in Fig. 8 are colour coded by their large-scale environment. We see a clear dependence on environment, where for fixed halo mass, more massive central galaxies reside preferentially in the denser environments. We also show the median of the distribution for the central galaxies in the most and the least dense environments (red and blue lines, respectively). Our results indicate that for both simulations, central galaxies in haloes below  $\sim 10^{12} h^{-1} M_{\odot}$  in the most dense environments are more massive than those in the least dense environments. This is directly related to the results of the halo occupancy, where dark matter haloes in the densest environments are more



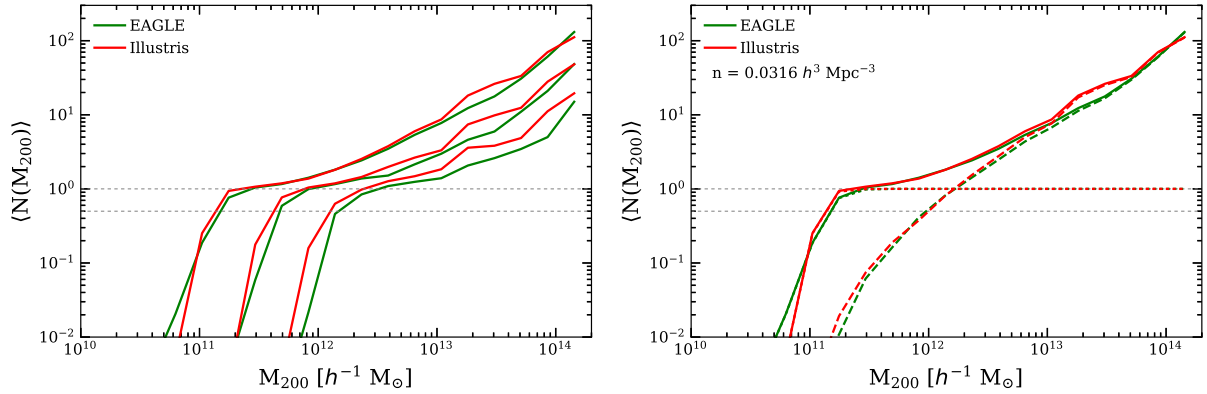


**Figure 5.** *Left panel:* The halo occupation functions of EAGLE galaxies (green lines) and Illustris (red lines) for the three number density cuts of  $n = 0.0316, 0.01, 0.00316 h^3 \text{Mpc}^{-3}$ , going from left to right. *Right panel:* The halo occupation functions of EAGLE and Illustris galaxies for the  $n = 0.0316 h^3 \text{Mpc}^{-3}$  sample, split by central (dotted lines) and satellite galaxies (dashed lines). The horizontal grey dotted lines can be used as reference to visually estimate  $M_1$  and  $M_{\text{min}}$  (see Appendix B).

likely to host central galaxies above a given stellar mass threshold than those dark matter haloes in the least dense environments.

This SMHM trend seems to be more significant and with less scatter for the hydrodynamical simulations studied in this work than in the semi-analytic models studied in Zehavi et al. (2018). This may be related to the apparent stronger occupancy variation signal in the hydrodynamical simulations compared to the semi-analytic models. However, we cannot make a detailed comparison here due to the different environment definitions used in Zehavi et al. (2018).

The SMHM dependence on halo formation time for central galaxies in EAGLE and Illustris is shown in Fig. 9. Black line shows the median value of the distribution with the 20% and 80% percentiles, while red and blue lines are the median of the distribution for those galaxies within the early-formed and late-formed haloes, respectively. The colour coding is done now by halo age. Our results show a wide range of formation times for the dark matter haloes below to  $\sim 10^{12} h^{-1} M_{\odot}$ , while massive haloes are in general late-formed, as also shown in Fig. 3. In both simulations, for the entire halo mass range studied, we find at fixed halo mass that central galaxies in early-formed haloes are more massive than those in late-formed haloes. This indicates that the halo formation time affects the occupancy of the haloes, in addition to halo mass.

Our findings thus show that, at fixed halo mass, there is a strong correlation between the age of the halo and the stellar mass of the central galaxy, as seen by the separation of the blue/red lines in Fig. 9. It arises since central galaxies in early-formed haloes have more time to accrete mass and form more stars and become more massive. This trend is slightly weaker when splitting the halo population by large-scale environment. As discussed in Zehavi et al. (2018), these results show that the stellar mass of the central galaxy depend on other properties besides the halo mass, directly giving rise to the central galaxy occupancy variation with halo formation time or environment.

## 6 SUMMARY AND CONCLUSIONS

In this work we study the signals of the occupancy variation of the HOD in the state-of-the-art hydrodynamical cosmological simulations EAGLE and Illustris. These occupancy variations coupled with halo assembly bias are what give rise to galaxy assembly bias. This work represents an extension of the recent study of Zehavi et al. (2018) with two semi-analytic models.

For each simulation, we compare the galaxy population within the dark matter haloes more massive than  $10^{10} h^{-1} M_{\odot}$  selected by large-scale environment and halo formation time. We define the large-scale environment of each halo by counting the number of subhaloes within a sphere of  $5 h^{-1} \text{Mpc}$  radius, while the halo formation time is estimated as the redshift for which the halo has assembled half of its present-day mass. In order to find the differences in the extreme cases, we select the 20% of the haloes in the most/least dense environment and the 20% latest/earliest formed haloes, in bins of halo mass. We analyse three fixed number density samples ranked by stellar mass corresponding to  $n = 0.0316, 0.01, 0.00316 h^3 \text{Mpc}^{-3}$ .

The comparison of the full HOD from EAGLE and Illustris at different number densities show that the mean occupation of haloes in Illustris is shifted towards lower halo masses relative to EAGLE (see Fig. 5). This can be explained by the differences in the halo mass functions of the simulations.

We find that the mean occupation of low mass haloes ( $\lesssim 10^{11} - 10^{12} h^{-1} M_{\odot}$ ) depends on the large-scale environment in both simulations, and this result is present for the three galaxy number densities selected. Thus, haloes in the densest regions are more likely to host a central galaxy than those in the least dense environments (Fig. 6). Moreover, the satellite occupation of the haloes shows a slight dependence on the large-scale environment, where the haloes in the densest regions have a mean occupation higher than those in least dense regions.

Examining the stellar mass – halo mass relation for the central galaxies, we find that, at a fixed dark matter halo mass below to  $10^{12} h^{-1} M_{\odot}$ , the central galaxies in the densest regions are more massive than those

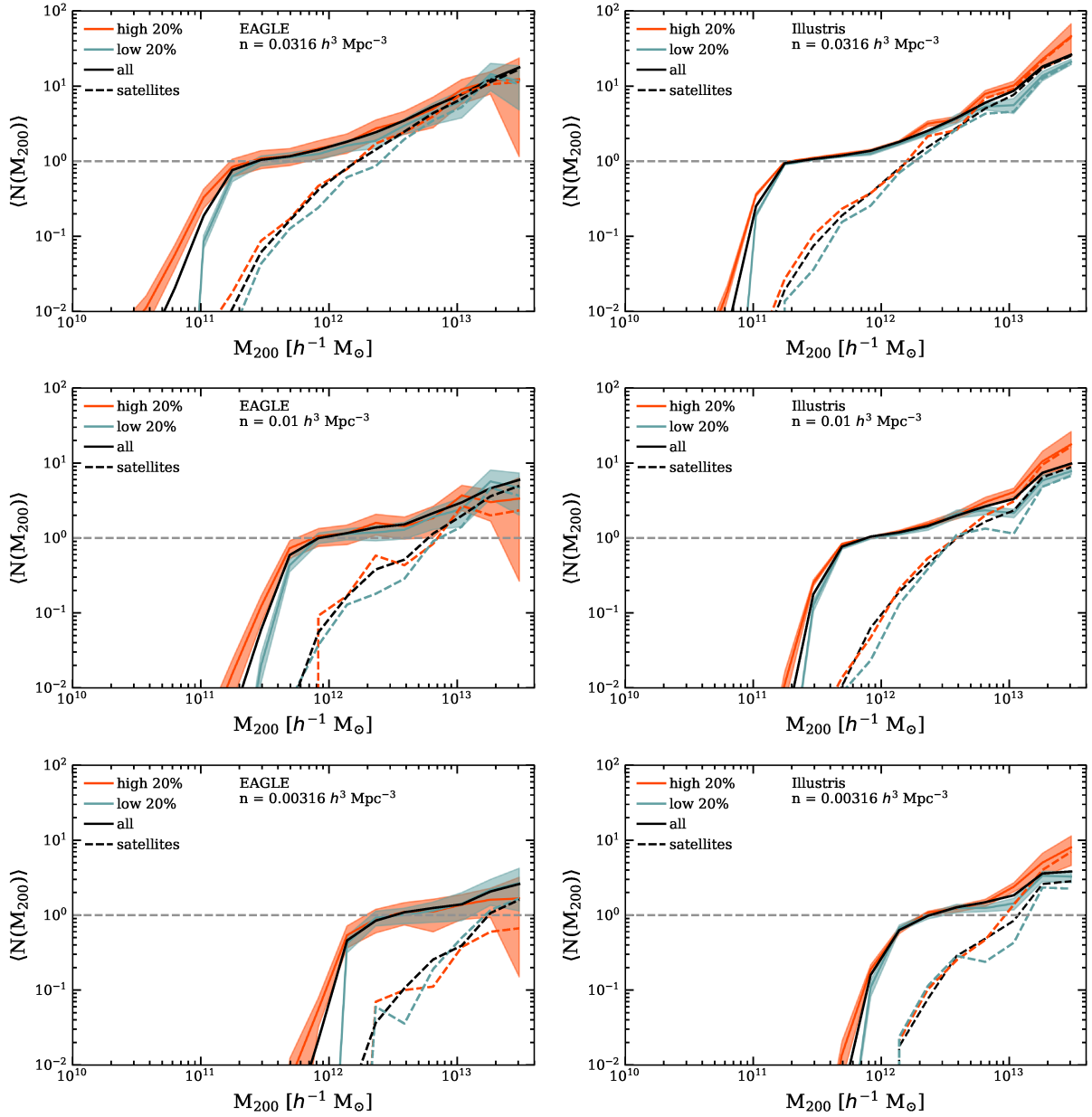


**Figure 6.** Halo occupation functions dependence on large-scale environment in EAGLE (*left panel*) and Illustris (*right panel*) for three number densities selected (high to low from top to bottom panel). Black solid lines represent the HOD of all galaxies in each sample. The red solid lines represent the HOD of the galaxies in the 20% of haloes in the densest regions, while the blue solid lines represent the HOD for the galaxies in the 20% of haloes in the least dense regions (following the definition described in Sec. 3). Error bars for the red and blue lines are computed via jack-knife resampling using 27 sub-volumes. Dashed lines represent the satellite occupancy functions for each sample.

in the least dense environments (Fig. 8). These results are present in both simulations, although EAGLE shows a stronger difference between the populations of haloes in least/most dense regions. Furthermore, our findings are in general agreement with the results presented in Zehavi et al. (2018) for semi-analytic galaxy formation models, and with those from McEwen & Weinberg (2018) using age-matching mock catalogues. This is in contrast with earlier analyses (Berlind et al. 2003; Mehta 2014) using different hydrodynamical simulations, which do not report the observed trends seen in this work. These differences perhaps have to

do with recent improvements in the stellar and AGN feedback models, and we plan to further investigate this in future work.

When we split the dark matter haloes by their formation time, we find a more significant difference in the halo occupation. Both simulations show that at low mass the early-formed (old) haloes are more likely to have a central galaxy than the late-formed (young) haloes, for the three cumulative number densities (see Fig. 7). This trend reverses at high masses due to the contribution of the satellite galaxies. Hence, we find that late-formed haloes host more satel-

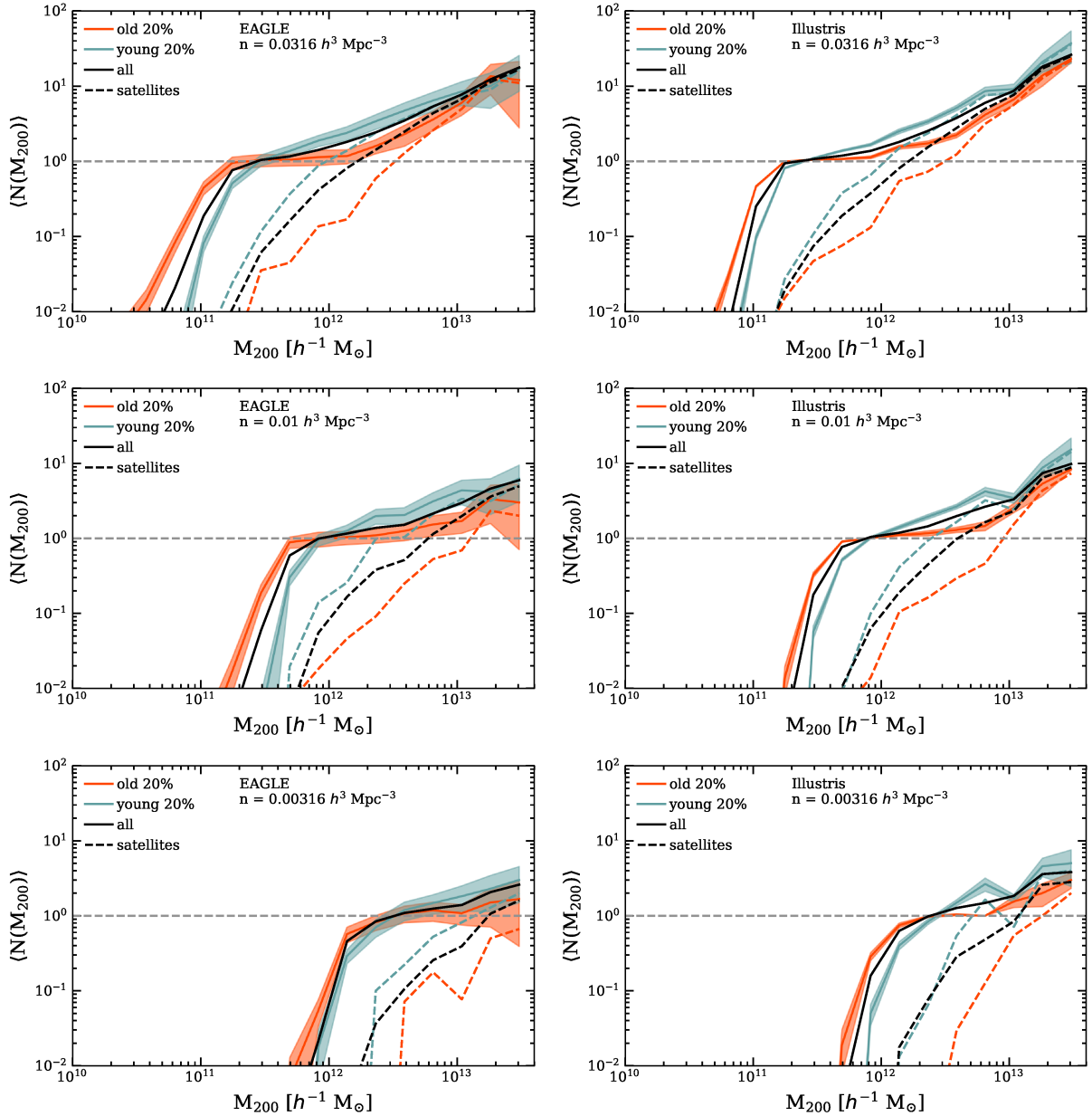


**Figure 7.** Halo occupation functions variation with halo formation time for EAGLE (*left panel*) and Illustris (*right panel*) for the three number densities selected  $n = 0.0316, 0.01, 0.00316 h^3 \text{Mpc}^{-3}$  (*top, middle and bottom panel*, respectively). Black solid lines represent the HOD of the galaxies in each sample. The red solid lines show the HOD for the galaxies in the 20% early-formed (old) haloes, while blue solid lines show the HOD for the galaxies in the 20% late-formed (young) haloes, following the definition described in Sec. 3. We include error bars for the red and blue lines computed through jack-knife resampling by using 27 slices of the full simulated volume. Dashed lines show the satellite occupancy functions for each sample.

lite galaxies than early-formed haloes. These results can be explained by the central galaxies having more time to assemble in the early-formed haloes. And in turn, the satellite galaxies have more time to merge with the central galaxy in early-formed massive haloes.

Finally, we study the SMHM relation in terms of halo formation time, finding that, at fixed mass, the early-formed haloes host more massive central galaxies than the late-formed haloes. This result supports the idea that early-formed haloes have more time to form a massive central galaxy and gives rise to the measured occupancy variations.

In agreement with previous findings by Zehavi et al. (2018), we find evidence of occupancy variation when splitting the haloes either by their formation time or by the large-scale environment, for both hydrodynamical simulations. Furthermore, we find that this signal is more significant when we split the halo population by age. These results provide robust predictions for occupancy variation from the latest state-of-the-art galaxy formation models. It remains to be determined what is the extent of occupancy variation and galaxy assembly bias in the real Universe.

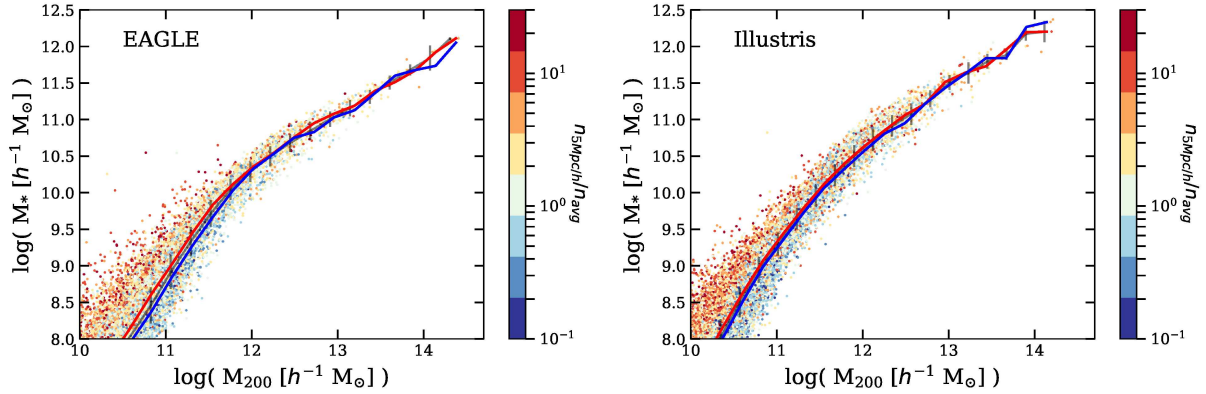


**Figure 8.** Stellar mass – halo mass relation for the central galaxies in EAGLE (*left panel*) and Illustris simulation (*right panel*), colour coded as a function of the environment of their haloes ( $n_{5\text{Mpc}/h}/n_{\text{avg}}$ ). Black lines represent the median value of the distribution with the error bars representing 20% and 80% percentiles. Red and blue lines show the median values for the galaxy samples within the most and least dense environments, respectively.

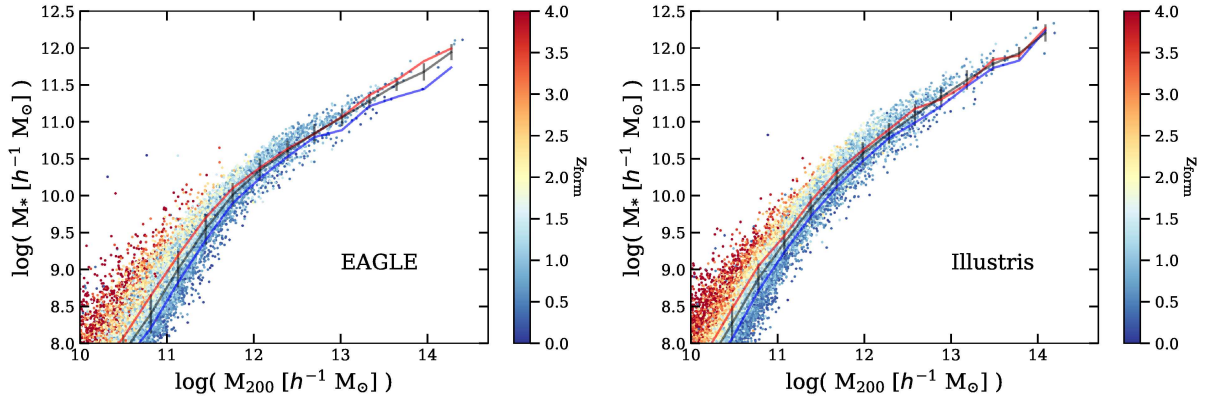


**Figure 9.** Stellar mass – halo mass relation for the central galaxies in EAGLE (*left panel*) and Illustris simulation (*right panel*), colour coded as a function of the formation time of their haloes ( $z_{\text{form}}$ ). Black lines represent the median value of the distribution with the error bars representing 20% and 80% percentiles. Red and blue lines show the median values for the galaxy samples within the early-formed and late-formed haloes, respectively.

## ACKNOWLEDGEMENT

We thank the anonymous referee for insightful comments. We also thank Carlton Baugh and Nelson Padilla for useful discussions and comments. MCA and SC acknowledge the Southern Astrophysics Network Proyecto Redes 150078 (Conicyt-Chile) for partial financial support, and the organizers of the first workshop held in Santiago de Chile where this project began. IZ acknowledges support by NSF grant AST-1612085. SC acknowledges support from a STFC/Newton-CONICYT Fund award (ST/M007995/1DPI20140114), Anillo ACT-1417 and the European Research Council through grant number ERC-StG/716151. PN acknowledges the support of the Royal Society through the award of a University Research Fellowship, and the Science and Technology Facilities Council (ST/P000541/1). We acknowledge the Virgo Consortium for making their simulation data available. The EAGLE simulations were performed using the DiRAC-2 facility at Durham, managed by the ICC, and the PRACE facility Curie based in France at TGCC, CEA, Bruyèresles-Châtel.

## REFERENCES

- Artale M. C., et al., 2017, *MNRAS*, **470**, 1771  
 Avila-Reese V., Colín P., Gottlöber S., Firmani C., Maulbetsch C., 2005, *ApJ*, **634**, 51  
 Baldry I. K., et al., 2012, *MNRAS*, **421**, 621  
 Behroozi P. S., Wechsler R. H., Wu H.-Y., 2013, *ApJ*, **762**, 109  
 Benson A. J., Cole S., Frenk C. S., Baugh C. M., Lacey C. G., 2000, *MNRAS*, **311**, 793  
 Berlind A. A., Weinberg D. H., 2002, *ApJ*, **575**, 587  
 Berlind A. A., et al., 2003, *ApJ*, **593**, 1  
 Blanton M. R., Berlind A. A., 2007, *ApJ*, **664**, 791  
 Booth C. M., Schaye J., 2009, *MNRAS*, **398**, 53  
 Bray A. D., et al., 2016, *MNRAS*, **455**, 185  
 Campbell D., van den Bosch F. C., Hearin A., Padmanabhan N., Berlind A., Mo H. J., Tinker J., Yang X., 2015, *MNRAS*, **452**, 444  
 Chabrier G., 2003, *PASP*, **115**, 763  
 Chaves-Montero J., Angulo R. E., Schaye J., Schaller M., Crain R. A., Furlong M., Theuns T., 2016, *MNRAS*, **460**, 3100  
 Conroy C., Wechsler R. H., Kravtsov A. V., 2006, *ApJ*, **647**, 201  
 Contreras S., Baugh C. M., Norberg P., Padilla N., 2013, *MNRAS*, **432**, 2717  
 Contreras S., Zehavi I., Baugh C. M., Padilla N., Norberg P.,

- 2017, *MNRAS*, **465**, 2833
- Crain R. A., et al., 2009, *MNRAS*, **399**, 1773
- Crain R. A., et al., 2015, *MNRAS*, **450**, 1937
- Croton D. J., Gao L., White S. D. M., 2007, *MNRAS*, **374**, 1303
- Dalal N., White M., Bond J. R., Shirokov A., 2008, *ApJ*, **687**, 12
- Dalla Vecchia C., Schaye J., 2012, *MNRAS*, **426**, 140
- Davis M., Efstathiou G., Frenk C. S., White S. D. M., 1985, *ApJ*, **292**, 371
- Di Cintio A., Brook C. B., Dutton A. A., Macciò A. V., Stinson G. S., Knebe A., 2014, *MNRAS*, **441**, 2986
- Di Matteo T., Springel V., Hernquist L., 2005, *Nature*, **433**, 604
- Dragomir R., Rodríguez-Puebla A., Primack J. R., Lee C. T., 2018, *MNRAS*, **476**, 741
- Dutton A. A., et al., 2016, *MNRAS*, **461**, 2658
- Dvornik A., et al., 2017, *MNRAS*, **468**, 3251
- Faltenbacher A., White S. D. M., 2010, *ApJ*, **708**, 469
- Furlong M., et al., 2015, *MNRAS*, **450**, 4486
- Gao L., White S. D. M., 2007, *MNRAS*, **377**, L5
- Gao L., Springel V., White S. D. M., 2005, *MNRAS*, **363**, L66
- Garaldi E., Romano-Díaz E., Borzyszkowski M., Porciani C., 2018, *MNRAS*, **473**, 2234
- Genel S., et al., 2014, *MNRAS*, **445**, 175
- Guo H., et al., 2014, *MNRAS*, **441**, 2398
- Haardt F., Madau P., 2001, in Neumann D. M., Tran J. T. V., eds, *Clusters of Galaxies and the High Redshift Universe Observed in X-rays*. ([arXiv:astro-ph/0106018](https://arxiv.org/abs/astro-ph/0106018))
- Hahn O., Porciani C., Dekel A., Carollo C. M., 2009, *MNRAS*, **398**, 1742
- Hearin A. P., Watson D. F., 2013, *MNRAS*, **435**, 1313
- Hearin A. P., Watson D. F., van den Bosch F. C., 2015, *MNRAS*, **452**, 1958
- Hearin A. P., Zentner A. R., van den Bosch F. C., Campbell D., Tollerud E., 2016a, *MNRAS*, **460**, 2552
- Hearin A. P., Behroozi P. S., van den Bosch F. C., 2016b, *MNRAS*, **461**, 2135
- Jiang F., van den Bosch F. C., 2017, *MNRAS*, **472**, 657
- Jiang L., Helly J. C., Cole S., Frenk C. S., 2014, *MNRAS*, **440**, 2115
- Kauffmann G., Li C., Zhang W., Weinmann S., 2013, *MNRAS*, **430**, 1447
- Lacerna I., Padilla N., Stasyszyn F., 2014, *MNRAS*, **443**, 3107
- Lehmann B. V., Mao Y.-Y., Becker M. R., Skillman S. W., Wechsler R. H., 2017, *ApJ*, **834**, 37
- Leja J., van Dokkum P., Franx M., 2013, *ApJ*, **766**, 33
- Mao Y.-Y., Williamson M., Wechsler R. H., 2015, *ApJ*, **810**, 21
- Mao Y.-Y., Zentner A. R., Wechsler R. H., 2018, *MNRAS*, **474**, 5143
- Matthee J., Schaye J., Crain R. A., Schaller M., Bower R., Theuns T., 2017, *MNRAS*, **465**, 2381
- McAlpine S., et al., 2016, *Astronomy and Computing*, **15**, 72
- McEwen J. E., Weinberg D. H., 2018, *MNRAS*, **477**, 4348
- Mehta K. T., 2014, PhD thesis, The University of Arizona
- Mitchell P. D., Lacey C. G., Baugh C. M., Cole S., 2013, *MNRAS*, **435**, 87
- Miyatake H., More S., Takada M., Spergel D. N., Mandelbaum R., Rykoff E. S., Rozo E., 2016, *Physical Review Letters*, **116**, 041301
- Montero-Dorta A. D., et al., 2017, *ApJ*, **848**, L2
- Mundy C. J., Conselice C. J., Owersworth J. R., 2015, *MNRAS*, **450**, 3696
- Nelson D., et al., 2015, *Astronomy and Computing*, **13**, 12
- Padilla N., Christlein D., Gawiser E., Marchesini D., 2011, *A&A*, **531**, A142
- Peacock J. A., Smith R. E., 2000, *MNRAS*, **318**, 1144
- Pedrosa S., Tissera P. B., Scannapieco C., 2010, *MNRAS*, **402**, 776
- Pillepich A., et al., 2018, *MNRAS*, **473**, 4077
- Planck Collaboration et al., 2014, *A&A*, **571**, A16
- Qu Y., et al., 2017, *MNRAS*, **464**, 1659
- Reddick R. M., Wechsler R. H., Tinker J. L., Behroozi P. S., 2013, *ApJ*, **771**, 30
- Reed D. S., Governato F., Quinn T., Stadel J., Lake G., 2007, *MNRAS*, **378**, 777
- Rodríguez-Gómez V., et al., 2015, *MNRAS*, **449**, 49
- Rosas-Guevara Y. M., et al., 2015, *MNRAS*, **454**, 1038
- Sales L. V., et al., 2015, *MNRAS*, **447**, L6
- Schaller M., et al., 2015, *MNRAS*, **451**, 1247
- Schaye J., 2004, *ApJ*, **609**, 667
- Schaye J., Dalla Vecchia C., 2008, *MNRAS*, **383**, 1210
- Schaye J., et al., 2010, *MNRAS*, **402**, 1536
- Schaye J., et al., 2015, *MNRAS*, **446**, 521
- Scoccimarro R., Sheth R. K., Hui L., Jain B., 2001, *ApJ*, **546**, 20
- Seljak U., 2000, *MNRAS*, **318**, 203
- Shen S., Mo H. J., White S. D. M., Blanton M. R., Kauffmann G., Voges W., Brinkmann J., Csabai I., 2003, *MNRAS*, **343**, 978
- Sheth R. K., Tormen G., 2004, *MNRAS*, **350**, 1385
- Snyder G. F., et al., 2015, *MNRAS*, **454**, 1886
- Springel V., 2005, *MNRAS*, **364**, 1105
- Springel V., 2010, *MNRAS*, **401**, 791
- Springel V., Hernquist L., 2003, *MNRAS*, **339**, 312
- Springel V., White S. D. M., Tormen G., Kauffmann G., 2001, *MNRAS*, **328**, 726
- Springel V., Di Matteo T., Hernquist L., 2005, *MNRAS*, **361**, 776
- Springel V., et al., 2018, *MNRAS*, **475**, 676
- Sunayama T., Hearin A. P., Padmanabhan N., Leauthaud A., 2016, *MNRAS*, **458**, 1510
- Tinker J. L., Conroy C., Norberg P., Patiri S. G., Weinberg D. H., Warren M. S., 2008, *ApJ*, **686**, 53
- Tinker J. L., Wetzel A. R., Conroy C., Mao Y.-Y., 2017, *MNRAS*, **472**, 2504
- Tinker J. L., Hahn C., Mao Y.-Y., Wetzel A. R., Conroy C., 2018, *MNRAS*, **477**, 935
- Tissera P. B., White S. D. M., Pedrosa S., Scannapieco C., 2010, *MNRAS*, **406**, 922
- Tojeiro R., et al., 2017, *MNRAS*, **470**, 3720
- Torrey P., et al., 2015, *MNRAS*, **454**, 2770
- Trayford J. W., et al., 2015, *MNRAS*, **452**, 2879
- Vakili M., Hahn C. H., 2016, preprint, ([arXiv:1610.01991](https://arxiv.org/abs/1610.01991))
- Vogelsberger M., Genel S., Sijacki D., Torrey P., Springel V., Hernquist L., 2013, *MNRAS*, **436**, 3031
- Vogelsberger M., et al., 2014, *MNRAS*, **444**, 1518
- Wang Y., Yang X., Mo H. J., van den Bosch F. C., Weinmann S. M., Chu Y., 2008, *ApJ*, **687**, 919
- Wang L., Weinmann S. M., De Lucia G., Yang X., 2013, *MNRAS*, **433**, 515
- Wechsler R. H., Bullock J. S., Primack J. R., Kravtsov A. V., Dekel A., 2002, *ApJ*, **568**, 52
- Wechsler R. H., Zentner A. R., Bullock J. S., Kravtsov A. V., Allgood B., 2006, *ApJ*, **652**, 71
- Wiersma R. P. C., Schaye J., Smith B. D., 2009a, *MNRAS*, **393**, 99
- Wiersma R. P. C., Schaye J., Theuns T., Dalla Vecchia C., Tornatore L., 2009b, *MNRAS*, **399**, 574
- Yang X., Mo H. J., van den Bosch F. C., 2006, *ApJ*, **638**, L55
- Zehavi I., et al., 2011, *ApJ*, **736**, 59
- Zehavi I., Contreras S., Padilla N., Smith N. J., Baugh C. M., Norberg P., 2018, *ApJ*, **853**, 84
- Zentner A. R., 2007, *International Journal of Modern Physics D*, **16**, 763
- Zentner A. R., Berlind A. A., Bullock J. S., Kravtsov A. V., Wechsler R. H., 2005, *ApJ*, **624**, 505
- Zentner A. R., Hearin A. P., van den Bosch F. C., 2014, *MNRAS*, **443**, 3044
- Zheng Z., et al., 2005, *ApJ*, **633**, 791
- Zhu G., Zheng Z., Lin W. P., Jing Y. P., Kang X., Gao L., 2006, *ApJ*, **639**, L5

Zu Y., Zheng Z., Zhu G., Jing Y. P., 2008, *ApJ*, **686**, 41  
 Zu Y., Mandelbaum R., Simet M., Rozo E., Rykoff E. S., 2017, *MNRAS*, **470**, 551  
 van den Bosch F. C., Tormen G., Giocoli C., 2005, *MNRAS*, **359**, 1029

## APPENDIX A: THE DEFINITION OF DENSITY ENVIRONMENT

In § 3 we define the criteria to select the dark matter haloes in dense and underdense environments. In summary, for each dark matter halo with  $M_{200} > 10^{10} h^{-1} M_{\odot}$ , we compute the number density within a sphere of fixed radius by counting the number of subhaloes using periodic boundary conditions, and excluding those within the halo ( $n_{R_{max}}$ ) and dividing by the volume of the sphere. We count the subhaloes within the sphere but outside of the halo itself since we want to measure the environment on large scales. This value is normalized by the mean number density of subhaloes in haloes of  $M_{200} > 10^{10} h^{-1} M_{\odot}$  ( $n_{avg}$ ). Thus, a ratio of one indicates that the halo resides in the average density environment. In particular, we then select the 20% of haloes in the most and least dense environments, thus providing a way to quantify and compare the halo occupation for the two extreme cases.

We check here the impact of the sphere radius used to calculate the environment. In order to discuss how robust is the radius selected, in Fig. A1 we show the distribution of the environment densities computed with three different thresholds in  $R_{max} = 3, 5, 8 h^{-1} \text{Mpc}$ . Our results show that the distributions obtained with the three different  $R_{max}$  are similar, finding only expected differences in the number  $N$  according to the radius, where the larger radius shows a slightly narrower distribution and more haloes within the average density environment.

We also test the impact of counting the subhaloes within each halo (i.e., for each halo we count all the subhaloes in the sphere irrespectively if they belong to the halo or not) finding that the distribution is not affected. Since we want to probe the large-scale environment, we would like to use a relatively large radius, significantly larger than the typical halo size. At the same time, that radius should not be too large, so as to maintain a reliable sampling of a large range of environments. Hence, we select the radius to be  $R_{max} = 5 h^{-1} \text{Mpc}$  as a compromise of these two considerations as well as taking into account the size limits of the simulation. This radius represents roughly seven per cent of the simulated box side for both EAGLE and Illustris.

## APPENDIX B: FITTING THE HOD PREDICTED BY EAGLE AND ILLUSTRIS

The HOD is commonly parametrized by making a distinction between central and satellite galaxies (e.g., Zheng et al. 2005; Zehavi et al. 2011; Contreras et al. 2013). For central galaxies, the mean occupation function can be described by a step-like function with a cut-off profile, while satellites follow a power-law function with a smooth cut-off at small halo masses. The most frequently used parametrization is the 5-parameter model introduced by Zheng et al. (2005). The model includes the quantities  $M_{min}$  and  $M_1$ , where  $M_{min}$

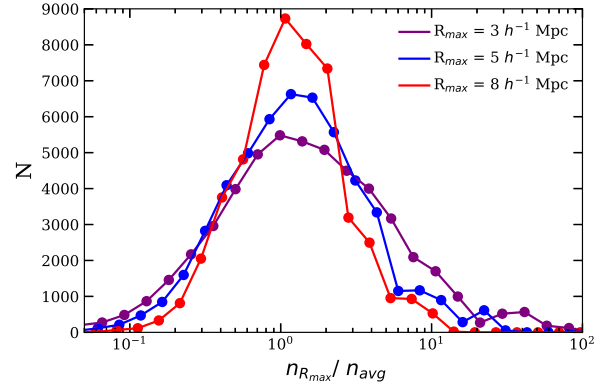


**Figure A1.** Distribution of the environmental densities of dark matter haloes with  $M_{200} > 10^{10} h^{-1} M_{sun}$ , in a sphere of  $R_{max} = 3, 5, 8 h^{-1} \text{Mpc}$  at  $z = 0$  (purple, blue and red, respectively). We compute the number of subhaloes within the sphere of  $R_{max}$  ( $n_{R_{max}}$ ), and normalize by the average number density of subhaloes in dark matter haloes of  $M_{200} > 10^{10} h^{-1} M_{sun}$  ( $n_{avg}$ ).

refers to the halo mass for which half of the haloes on average host a central galaxy (i.e.,  $\langle N_{cen}(M_{min}) \rangle = 0.5$ ), while  $M_1$  is the mass at which the halo has on average one satellite galaxy (i.e.,  $\langle N_{sat}(M_1) \rangle = 1$ ). The ratio of these quantities ( $M_1/M_{min}$ ) gives us information about how much larger the dark matter halo mass has to be in order to host an additional satellite galaxy beyond the central one. Hence a larger value of the ratio implies a wider range of halo masses hosting just a central galaxy (Berlind et al. 2003). Furthermore, it influences the shape of the correlation function and reflects the balance between accretion and destruction of satellite galaxies (Zentner et al. 2005).

The halo occupation function is commonly modelled in the following form (following Contreras et al. 2017; Zehavi et al. 2018). For central galaxies:

$$\langle N_{cen}(M_h) \rangle = \frac{1}{2} \left[ 1 + \text{erf} \left( \frac{\log M_h - \log M_{min}}{\sigma_{\log M}} \right) \right], \quad (\text{B1})$$

where  $\sigma_{\log M}$  reflects the scatter between the halo and stellar mass, and  $\text{erf}(x)$  is the error function,  $\text{erf}(x) = \frac{2}{\sqrt{\pi}} \int_0^x e^{-t^2} dt$ . For satellite galaxies, we use:

$$\langle N_{sat}(M_h) \rangle = \left( \frac{M_h - M_{cut}}{M_1^*} \right)^\alpha, \quad (\text{B2})$$

where  $\alpha$  is the slope of the power-law,  $M_{cut}$  is the satellite cut-off mass scale, and  $M_1^*$  is the normalization with,  $M_1 = M_1^* + M_{cut}$ . Therefore, the total halo occupation function is given by the sum of these two terms:

$$\langle N_{gal}(M_h) \rangle = \langle N_{cen}(M_h) \rangle + \langle N_{sat}(M_h) \rangle. \quad (\text{B3})$$

We note that the model we implement, originally proposed by Zheng et al. (2005), allows to fit the central and satellite occupation functions independently. In Tables B1 and B2 we present the values obtained for these five parameters of the halo occupation function for EAGLE and Illustris. We fit the HOD for central and satellite galaxies separately, and assume equal weight to all measurements in the halo mass range that fulfills the condition of  $\langle N(M_h) \rangle = 10^{-1.0} - 10^{1.5}$ . The fits are computed using the

HOD with halo mass bins of  $\sim 0.24$  dex, the same as shown before. We derive the errors from jack-knife resampling, using 27 sub-volumes for each simulation. We find that  $M_1$  and  $M_{\min}$  increase as the number density cut decreases in both simulations. This is expected since a lower number density corresponds to a higher stellar mass cut. This is also the case for  $M_{\text{cut}}$ . We note here that the halo masses  $M_h$  implemented to compute the HOD correspond to those from the hydrodynamical simulations and not to their DMO counterparts. Hence, although we expect a negligible difference when using DMO halo masses, it is important to consider this aspect when comparing our findings with, for example, SHAM models (see [Chaves-Montero et al. 2016](#)).

For the ratio  $M_1/M_{\min}$  we find different trends and values. For Illustris the ratio decreases with the number density, in agreement with previous results from observations and semi-analytic models (e.g., [Guo et al. 2014](#); [Contreras et al. 2017](#)), while for EAGLE the trend reverses. These results indicate that massive central galaxies, which reside in the more massive haloes, are more likely to be accompanied by a satellite galaxy in Illustris than in EAGLE. We are unsure what is the cause of the reversed trend of  $M_1/M_{\min}$  in the simulations studied. It is also important to note that slight changes in the parameters  $M_1$  and  $M_{\min}$  result in different trends for the ratio, which further indicates that this trend should be regarded with caution.

### APPENDIX C: SUBSTRUCTURE OCCUPANCY VARIATION

We show in Sec. 4.2 that haloes in the most dense environments are more likely to host a higher amount of satellites than those in the least dense environments, and in Sec. 4.3 that late formed haloes contain a higher mean number of satellites than early formed haloes. Given these results, it is interesting to explore our findings in the context of the subhalo occupancy variation. This is particularly relevant for SHAM techniques.

The simplest form of SHAM connects subhaloes with galaxies using a monotonic relation between a subhalo property such as the maximum circular velocity,  $V_{\text{max}}$ , or the infall mass, and a galaxy property like the stellar mass or luminosity. We note however that most SHAM models tend to include some additional scatter in this relation to create a model that reproduces the data well enough.

To some extent it should be expected that SHAM models will contain some subhalo occupancy variation signal (e.g., [Zentner et al. 2014](#); [Chaves-Montero et al. 2016](#)). First, it is well established that haloes with higher concentration have a larger  $V_{\text{max}}$  than less concentrated ones ([Wechsler et al. 2002, 2006](#)). Moreover, haloes with higher concentration assemble earlier. This makes it more likely for SHAM models to host galaxies in early formed haloes. Furthermore, haloes with higher concentrations contain less subhaloes compared to less concentrated ones ([Zentner et al. 2005](#); [Mao et al. 2015](#)), as subhaloes in early formed haloes have more time to merge and/or deplete through dynamical friction.

In this appendix, we investigate the occupancy variation in the context of subhaloes and galaxies. For this, we use the EAGLE simulation with the halo population split by

environment and formation time (see respectively § 3.1 and 3.2 for further details). To compare the halo occupancy of subhaloes and satellites, we adopt a cumulative number density cut of  $n = 0.0316 h^3 \text{ Mpc}^{-3}$ , one of the thresholds used in § 4. The two samples are created by ranking satellite galaxies by stellar mass and subhaloes by  $V_{\text{max}}$ . We note that the halos considered by both samples are not necessarily the same as there is some scatter in the subhalo  $V_{\text{max}}$  and satellite stellar mass relation.

Fig. C1 shows our results split by halo environment and halo formation time (left and right panels respectively). In the top row we present the HOD for subhaloes (dotted curves) and satellites (dashed curves) of the EAGLE simulation, including the various sample splits (see figure key). Similar to our results for satellite galaxies in Sec. 4.2 and Sec. 4.3, we find that haloes in denser environments (or formed late) host on average more subhaloes than those in less dense environments (or formed early). The middle row shows the ratio of the average number of satellites per halo and the average number of subhaloes per halo as function of halo mass (in effect the ratio of the same coloured lines in the top panel). This ratio highlights further differences in the HOD of satellites and subhaloes. To quantify their significance, we estimate the relative error on the ratio assuming maximally anti-correlated Poisson statistics for the satellite and subhalo distributions. This provides a simple upper limit to the relative error on the ratio, which for convenience is plotted around the line of equal satellite and subhalo occupancy. At large halo masses (above  $\sim 10^{12} h^{-1} M_{\odot}$ ), there are significantly more satellites than subhaloes for the cumulative number density cut considered. This is primarily due to the existing scatter in the subhalo  $V_{\text{max}}$  and satellite stellar mass relation.

In the bottom panel of Fig. C1, we show the satellite/subhalo occupancy variation, as given by the ratio of the HOD of satellites/subhaloes from subsamples split by formation time (environment) and the HOD of satellites/subhaloes from the full sample. Like in the middle panel, we estimate the significance assuming Poisson statistics, but this time we consider the maximally correlated Poisson statistic and plot the smallest one of the four options as reference around the line of no occupancy variation. This provides a simple lower limit to the relative error on the ratios. Hence in the EAGLE simulation, we show that, for the cumulative number density cut considered, the occupancy variations of subhaloes (dotted lines) do not show any significant differences with respect to the occupancy variations of satellite galaxies (dashed lines).

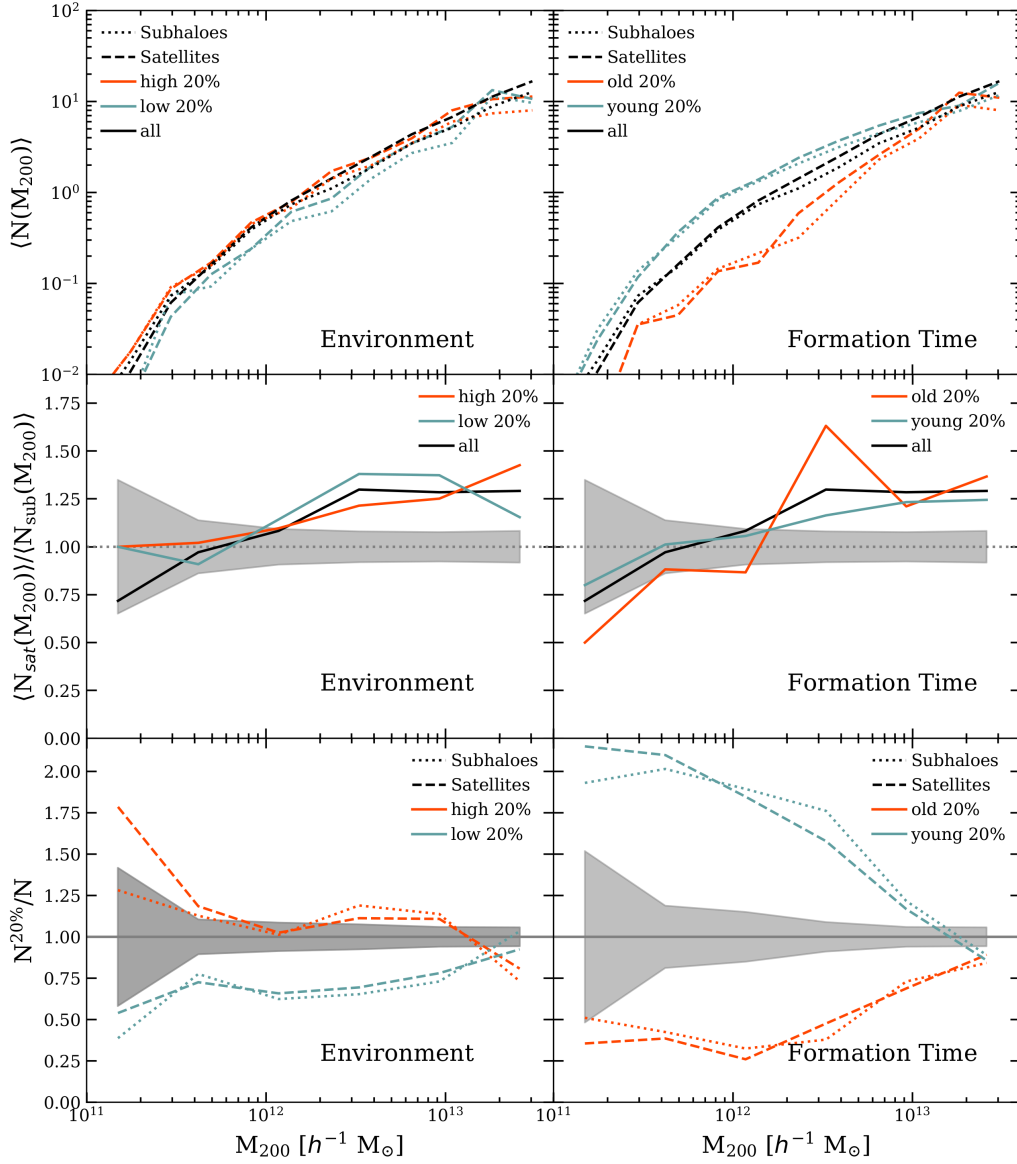


**Figure C1.** Comparison of satellite and subhalo occupancy in the EAGLE simulation for a cumulative density cut of  $n = 0.0316 h^3 \text{Mpc}^{-3}$ . The halo population is split by environment (left panel) and formation time (right panel; see § 3.1 and 3.2 for their definitions). The top panels show the HOD for each sample of subhaloes (dotted lines) and satellites (dashed lines; see color code in the figure key). The middle panels present the ratio between the HOD of satellites and subhaloes ( $\langle N_{sat}(M_{200}) \rangle / \langle N_{sub}(M_{200}) \rangle$ ) for the complete sample (black line) and according to environment and formation time (as shown by color code in panel key). The shaded grey area, centered on one, is used as reference to indicate the significance of the trends (see text for further details). The bottom panels show the occupancy variation of satellites (dashed lines) and subhaloes (dotted lines) of the subsamples compared to the reference sample ( $N^{20\%}/N$ ). The shaded grey area has the same role as in the middle panel (see text for further details). Our results show that the occupancy variations of subhaloes in the EAGLE simulation do not show any significant differences with respect to the occupancy variations of satellite galaxies.



**Table B1.** Values of the HOD parameters obtained from fitting the mean occupation function for satellites and central galaxies of EAGLE. The units of  $M_{\text{cut}}$ ,  $M_1$  and  $M_{\text{min}}$  are in  $h^{-1}M_{\odot}$ . We present our results for the three number densities selected. The errors are computed through jack-knife resampling.

n [ $h^3 \text{ Mpc}^{-3}$ ]	EAGLE					
	$\alpha$	$\log M_{\text{cut}}$	$\sigma_{\log M}$	$\log(M_1)$	$\log(M_{\text{min}})$	$M_1/M_{\text{min}}$
$3.16 \times 10^{-2}$	$0.92 \pm 0.03$	$11.49 \pm 0.05$	$0.202 \pm 0.006$	$12.21 \pm 0.01$	$11.149 \pm 0.005$	$11.51 \pm 0.43$
$1.00 \times 10^{-2}$	$1.08 \pm 0.12$	$11.34 \pm 0.81$	$0.243 \pm 0.017$	$12.78 \pm 0.03$	$11.656 \pm 0.009$	$13.30 \pm 0.84$
$3.16 \times 10^{-3}$	$1.17 \pm 0.18$	$11.90 \pm 1.82$	$0.318 \pm 0.031$	$13.32 \pm 0.04$	$12.166 \pm 0.015$	$14.25 \pm 1.17$

**Table B2.** Values of the HOD parameters obtained from fitting the mean occupation function for satellites and central galaxies of Illustris. The units of  $M_{\text{cut}}$ ,  $M_1$  and  $M_{\text{min}}$  are in  $h^{-1}M_{\odot}$ . We present our results for the three number densities selected. The errors are computed through jack-knife resampling.

n [ $h^3 \text{ Mpc}^{-3}$ ]	Illustris					
	$\alpha$	$\log M_{\text{cut}}$	$\sigma_{\log M}$	$\log(M_1)$	$\log(M_{\text{min}})$	$M_1/M_{\text{min}}$
$3.16 \times 10^{-2}$	$1.09 \pm 0.11$	$11.26 \pm 0.21$	$0.152 \pm 0.002$	$12.22 \pm 0.02$	$11.094 \pm 0.002$	$13.36 \pm 0.72$
$1.00 \times 10^{-2}$	$0.99 \pm 0.05$	$11.86 \pm 0.10$	$0.195 \pm 0.006$	$12.62 \pm 0.02$	$11.598 \pm 0.003$	$10.52 \pm 0.44$
$3.16 \times 10^{-3}$	$1.09 \pm 0.11$	$11.69 \pm 5.62$	$0.251 \pm 0.021$	$13.06 \pm 0.03$	$12.094 \pm 0.011$	$9.25 \pm 0.70$